THE JOURNAL OF PHYSICAL CHEMISTRY C

Article

pubs.acs.org/JPCC

Quantitative Nanoscale Mapping with Temperature Dependence of the Mechanical and Electrical Properties of Poly(3-hexylthiophene) by Conductive Atomic Force Microscopy

Dawn Wood,[†,‡] Ian Hancox,[†] Tim S. Jones,[†] and Neil R. Wilson*[,‡]

[†]Department of Chemistry and [‡]Department of Physics, University of Warwick, Coventry, United Kingdom CV4 7AL

Supporting Information

ABSTRACT: Using conductive atomic force microscopy, we introduce a method to simultaneously acquire electrical space-charge-limited current measurements and material properties such as Young's modulus and surface adhesion with nanoscale resolution. We demonstrate the utility of this method using thin films of the prototypical, semiconducting polymer poly(3-hexylthiophene) (P3HT). Arrays of force−distance and current−voltage curves are acquired simultaneously, allowing the investigation of spatial heterogeneity and statistical analysis of correlations between material properties. Tip−surface contact mechanics are used to calculate the contact areas, allowing the accurate quantification of charge transport properties through the fitting of space-charge-limited current to a modified Mott−Gurney model to extract the charge transport mobility accurately at each point. Measurements were taken from room temperature to 140 °C under a constant nitrogen flow to investigate changes in the properties of P3HT under standard annealing conditions. The quantitative analysis of temperature-dependent charge transport and mechanical properties of P3HT is consistent with grain boundary limited transport models and shows qualitatively different behavior for annealed and unannealed samples. The acquisition and analysis procedures developed here are generally applicable to the study of a wide range of organic semiconductor thin films.

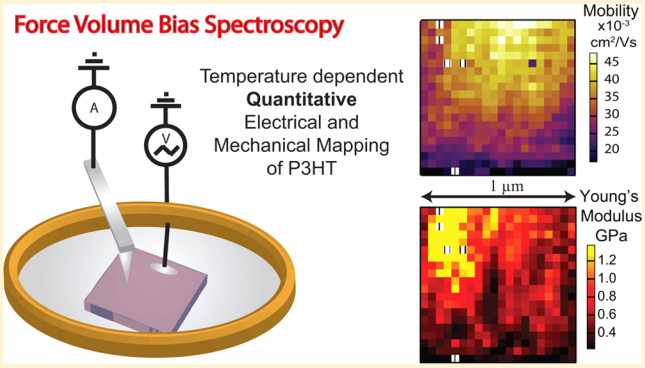

INTRODUCTION

Organic semiconductors (OSC) are comparatively cheap and easy to process into thin film devices for a wide variety of applications including organic light emitting diodes, organic thin film transistors (OTFTs), and organic photovoltaic cells (OPVs). However, device performance with OSCs is often limited by their low charge carrier mobility and its dependence on processing parameters. In addition, charge transport through thin film organic semiconductor devices is known to be heterogeneous at the nanoscale, due in part to heterogeneity in the electrode material typically used[1] but also due to changes in structure such as local crystallization of the OSC.[2]

Regioregular poly(3-hexylthiophene) (P3HT) is a widely studied, conjugated polymer OSC that is commonly used in OPVs[2,3] and OTFTs,[4,5] with a carrier mobility that is dependent on the degree of regioregularity, type of casting solvent, carrier concentration, molecular weight,[6,7] and postprocessing treatments such as thermal[8,9] and chemical annealing.[10] It is thought that the change in thin film structure induced by these modifications is the underlying cause of the mobility changes.[7,11] These structural changes result in, and can be observed by, changes in mechanical properties. For example, the Young's modulus of polythiophenes has been shown to be higher after annealing,[12] indicating a more crystalline, closer-packed phase.[13,14] In addition, correlations have been observed between the "bulk" electrical and mechanical properties of polythiophenes.[15] Understanding and developing these materials thus requires the development of techniques that can directly and simultaneously measure charge transport properties and correlate them to material properties with nanoscale resolution.

Conductive atomic force microscopy (cAFM) is a powerful technique for studying nanoscale heterogeneity in the conductivity of thin films.[16] Standard cAFM is performed by scanning a conductive tip across a sample at a fixed voltage and recording a current map simultaneously with the topography, with the current flowing between the conductive tip and a conductive back-electrode. This gives high spatial resolution but, due to the uncertainty in the tip−surface contact and the limitations of two-electrode transport measurements, it is difficult to derive quantitative information on the charge transport properties of the thin film material. Also, large lateral forces can lead to significant surface damage while scanning soft samples. Instead, cAFM can be used to measure the current as a function of voltage (current−voltage) with the tip held in place on the surface, again giving nanoscale resolution. Reid et al.

Received: March 6, 2015
Revised: April 27, 2015
Published: April 27, 2015

DOI: 10.1021/acs.jpcc.5b02197
J. Phys. Chem. C 2015, 119, 11459−11467

showed that by taking proper consideration of the experimental geometry, the charge transport mobility can be quantitatively determined by fitting the measured current−voltage curves in the space-charge-limited regime to a modified Mott−Gurney equation.[17] MacDonald et al. extended this to move beyond single point measurements.[1] In a way analogous to how force−volume mapping applies an array of single point force−distance measurements to create a spatially resolved map of nanomechanical properties, Macdonald et al. applied an array of single point current−voltage measurements to form a spatially resolved map of charge transport properties (scanning current spectroscopy, SCS).[1] Fitting each current−voltage curve to a modified Mott−Gurney model, they showed that the interface between the OSC thin film and the transparent conductive oxide back-electrode was heterogeneous and often limited device performance.

The combination of nanoscale spatial resolution and quantitative charge transport analysis makes SCS a powerful technique for studying transport in thin film organic semiconductors. However, there are limitations: the accuracy with which the charge transport parameters can be quantified is limited by uncertainty in the contact area between the tip and the surface, and SCS on its own does not give information on the local structure and mechanical properties of the OSC. Nikiforov and Darling made progress in this area by combining nanomechanical mapping with cAFM, allowing correlations to be made between mechanical properties and thin film conductivity.[18] They also showed that, under certain assumptions about the contact mechanics, the contact area could be determined directly from the nanomechanical measurements thus eliminating the major uncertainty in the conductivity measurements,[18] although they could not derive quantitative measures of mobility as only fixed voltage measurements were made. These combined nanoelectrical and nanomechanical measurements offer the potential for deeper insight into the operation and development of OSCs.

Here, we quantitatively and simultaneously map the electrical and mechanical properties of P3HT with nanoscale resolution, using the mechanical measurements to accurately determine the tip−surface contact area at each point. Furthermore, we study the evolution of these properties with increasing temperature, replicating in the AFM the standard thermal annealing conditions for P3HT. These results give insight into the heterogeneous charge transport properties of P3HT, showing that charge transport and mechanical properties vary significantly over length scales of tens of nanometers.

EXPERIMENTAL SECTION

Device Fabrication. Indium tin oxide (ITO) -coated glass substrates (Thin Film Devices, 145 nm ITO thickness) were solvent-cleaned and treated in ultraviolet light and ozone to remove carbon residues. Metal oxide hole transporting layers, MoO_x [MoO_3 (Aldrich, 99.99%)] were grown by thermal evaporation under vacuum in a Kurt J. Lesker Spectros system with a base pressure of 8×10^{-8} mbar onto the freshly cleaned ITO. Active layers were deposited from 20 mg/mL P3HT (Rieke, >98% regioregular, MW = 25 kDa), dissolved in anhydrous 1,2-dichlorobenzene (Sigma-Aldrich, 99%) and stirred for 48 h at 40 °C under a N_2 atmosphere, by spin-coating onto the MoO_x hole transporting layer at 1200 rpm under an N_2 atmosphere. Where stated, samples were annealed at 140 °C for 20 min in nitrogen. Thicknesses of the layers: P3HT, 100 nm; MoO_x, 8 nm; ITO, 145 nm.

Atomic Force Microscopy. AFM maps were obtained using an Asylum Research MFP-3D (Santa Barbara, CA) at a set point force between 10 and 20 nN. Temperature was controlled in situ using an Asylum Research Polyheater (Santa Barbara, CA) with an input N_2 flow of 0.4 L/min. For the results shown in Figure 8, the heating rate between the fixed temperature measurements was 10 °C/min. After increasing the sample temperature, we incorporated a delay of 20 min to allow thermal equilibrium to be reached before FVBS measurements; during cooling, the delay was increased to 30 min. Olympus AC240TM-R3 (Ti−Pt coated) AFM cantilevers were used (nominal resonance frequency of 70 kHz and nominal spring constant of 2.1 N/m). Rocky Mountain Nanotechnology 25PT300B probes (full metal Pt) with a nominal resonance frequency of 20 kHz and spring constant of 18 N/m were used to obtain the measurements displayed in Figure 6 (E_t = 168 GPa and ν_t = 0.38).[19] Cantilevers were calibrated using the Sader method,[20] and fresh tips were used for each sample. The DAC/ADC offsets were calibrated using the procedure described by Reid et al.[17]

Data Analysis. Data analysis was automated within the Igor Pro software used for control of the AFM hardware. Further details of the fitting procedures are available in the Supporting Information.

RESULTS

Force−Distance and Current−Voltage Acquisition from P3HT. Thin film samples of P3HT on ITO were prepared by spin coating in a nitrogen environment, as described in the Experimental Section. A thin molybdenum oxide layer was included between the ITO and P3HT, acting as a high work function hole transport layer.[21,22] With this configuration, charge transport occurred through hole transport from the ITO back-electrode through the P3HT thin film and was collected by a Pt-coated AFM tip used as the top electrode. The current flow was measured by a virtual earth current amplifier close to the tip, with the bias voltage applied to the back-electrode (indium tin oxide, ITO); a positive bias voltage here means that the back-electrode is positively biased relative to the tip. A schematic of the sample and cAFM setup is shown in Figure 1.

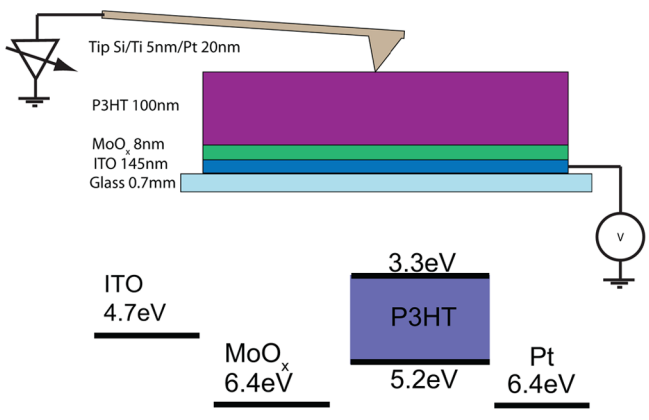

Figure 1. (Top) schematic of the experimental geometry. (Bottom) schematic energy level diagram of the materials involved. The workfunctions of ITO, MoO_x, and Pt are shown in relation to the highest occupied molecular orbital (HOMO) and lowest unoccupied molecular orbital (LUMO) of P3HT.

DOI: 10.1021/acs.jpcc.5b02197
J. Phys. Chem. C 2015, 119, 11459−11467

SCS is combined with conventional force−volume mapping, generating an array of force−distance and current−voltage measurements acquired on a regularly spaced two-dimensional grid. We refer to this technique as force−volume bias spectroscopy (FVBS). The procedure for acquiring simultaneous force−distance and current−voltage data at each single point was as follows: (1) the cantilever was approached toward the surface at a constant rate until a predefined set point value of deflection, or trigger point, was reached (approach/loading); (2) the tip was held in position with the feedback loop on to maintain constant deflection while the current−voltage data were acquired (dwell); (3) the cantilever was retracted away from the surface (unloading/retract). The deflection and z position were acquired at all times, and the applied bias voltage was zero during the approach and retraction. After each point measurement, the x, y position was changed according to the required grid, and the single point measurement was repeated.

Typical data for a single force−distance/current−voltage acquisition on P3HT, acquired at 70 °C, are shown in Figure 2.

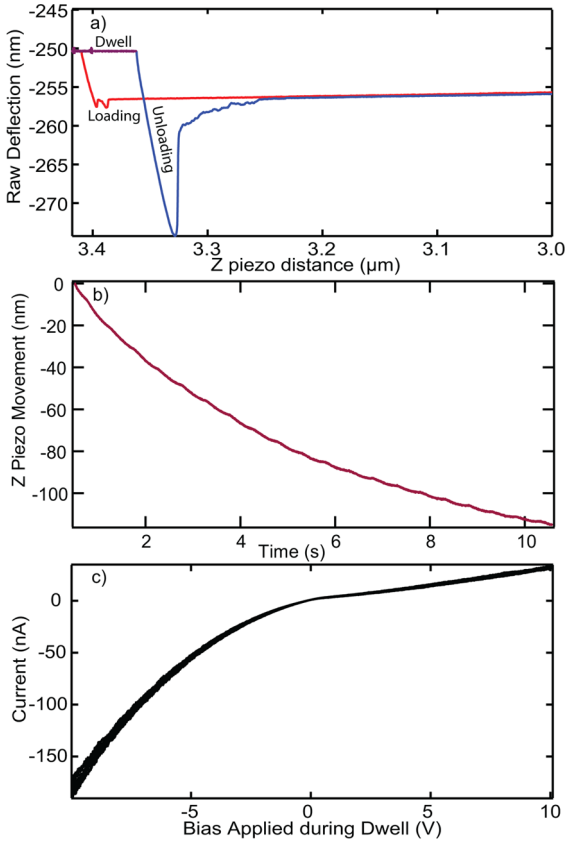

Figure 2. (a) Typical force curve displaying three sections of data as labeled. (b) Expanded dwell section, transposed into z piezo movement while the force is constant against the time held. (c) $I-V$ curves acquired during the dwell.

Figure 2a shows the expected behavior during loading (the approach curve), with the tip jumping onto the surface when the gradient of the attractive tip−surface forces exceeds the spring constant of the cantilever. Once in contact, the relatively low slope of loading is indicative of indentation on a soft sample.[23] During the dwell stage (Figure 2b), the tip was held against the surface with a constant force. Analysis of the indentation creep under the same conditions has been shown to give information on the viscoelastic parameters of polymers.[24] However, we found no evidence in the force−distance curves for viscoelastic deformation during the dwell stage, indicating that the P3HT was deforming elastically (the small observed changes in z piezo displacement can be attributed to thermal drift due to differential thermal expansion). During this dwell stage, the current was measured as a function of applied voltage ($I-V$), with 10 $I-V$ curves acquired during each dwell. The $I-V$ curves acquired were asymmetric (Figure 2c), as is commonly found in cAFM even for nominally electronically symmetric structures.[25] Here, the higher current flow at a negative bias indicates that hole injection was more efficient through the platinum tip than the MoO_x/ITO substrate.

During unloading, the retract curve shows hysteresis as expected due to adhesion forces keeping the tip in contact with the surface until the pull-off force is reached. The magnitude of the adhesion force is determined here by the minimum force prior to jump-off contact.

An important parameter in the setup of these measurements is the trigger point for the deflection. This defines the force applied during the acquisition of the current−voltage data, which here is typically 10 nN. This was found to be enough force to maintain a stable electrical contact while minimizing surface damage.

After acquisition, the deflection versus z displacement data were converted to force versus indentation ($F-\delta$) data and the current versus voltage data to current density versus voltage ($J-V$) data. Each $F-\delta$ and $J-V$ curve can then be fitted by an appropriate model to quantitatively extract the mechanical and electrical properties.

Analysis of Force−Distance Data. Conversion from deflection versus z displacement data to force versus indentation data requires accurate determination of the cantilever spring constant, the optical lever sensitivity, and the zero points for force and indentation. The procedures followed to achieve this are described in the Experimental Section and in section S1 in the Supporting Information.

As discussed above, the force versus distance curves show elastic deformation with significant adhesive force on a soft sample. For quantitative analysis, the adhesive force F_{ad} was determined by the minimum in the force prior to jump-off contact, and the unloading/retract force versus indentation data were fitted to extract the mechanical properties of the material. Various models are commonly used in the literature, such as the Hertz model (elastic deformation without adhesion), the Derjaguin−Muller−Toporov model (elastic deformation with adhesion, applicable for small tips and soft samples with small adhesion), and the Johnson−Kendall−Roberts (JKR) model (elastic deformation with adhesion, applicable for large tips and soft samples with a large adhesion).[23] Here the sample is soft with large adhesion, and so the data were fit by the JKR model. The JKR model predicts that the indentation, δ, depends on the applied force, F:

$$\delta = \frac{1}{r_{tip}}\left(\frac{r_{tip}}{E_{tot}}\left[\sqrt{F_{ad}} + \sqrt{F + F_{ad}}\right]^2\right)^{2/3} - \frac{4}{3}\sqrt{\frac{F_{ad}\left(\frac{r_{tip}}{E_{tot}}\left[\sqrt{F_{ad}} + \sqrt{F + F_{ad}}\right]^2\right)^{1/3}}{E_{tot} r_{tip}}} \quad (1)$$

where E_{tot} is the reduced Young's modulus of the tip and the sample given by

DOI: 10.1021/acs.jpcc.5b02197
J. Phys. Chem. C 2015, 119, 11459−11467

$$\frac{1}{E_{tot}} = \frac{3}{4}\left(\frac{1-\nu_t^2}{E_t} + \frac{1-\nu_s^2}{E_s}\right) \quad (2)$$

and r_{tip} is the radius of the tip. Known values from the literature were used for the mechanical properties of the tip (Young's modulus E_t = 169 GPa and Poisson's ratio ν_t = 0.22)[26]. Previous work has found the Poisson's ratio for P3HT ν_s = 0.35[26] (note that E_{tot} is relatively insensitive to small changes in ν_s).

Figure 3 shows the fit of eq 1 to experimental $F-\delta$ data (as in Figure 2). The fit yields values for E_{tot} and r_{tip}. Given these

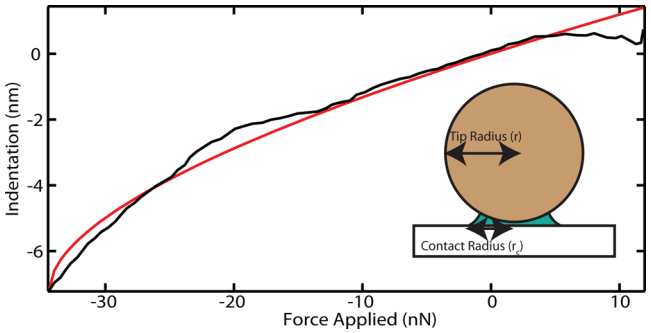

Figure 3. JKR fitting (red line) as applied to the unloading section of the retract curve (black line). Inset: schematic of the contact when unloading, as described by the JKR model.

values, it is then possible to determine the sample stiffness, E_s, using eq 2 and the contact area during the dwell, i.e., during the acquisition of the current versus the voltage data. Again using the JKR model, which accounts for the elastic deformation of the sample around the tip as shown in the inset in Figure 3, the contact radius (r_c) is given by

$$r_c = \left(\frac{r_{tip}}{E_{tot}}\left[\sqrt{F_{ad}} + \sqrt{F_{dwell} + F_{ad}}\right]^2\right)^{1/3} \quad (3)$$

where the average of the force measured during the dwell (see Figure 2b) gives F_{dwell}. It should be noted that the JKR model assumes that the radius of contact is smaller than the radius of the tip, as shown in the Figure 3 inset. Although this is not always the case in the data shown below, the JKR model gives a simple framework within which to model the experimental data and is likely to be accurate to within the precision of the experimental measurements. It is also important to note that not every force curve acquired was well fitted by the JKR model. For the analysis of the current–voltage data described in the next section, poorly fitted force curves were ignored and their contact area taken as the average contact area of all of the fitted curves at the same temperature.

Within the constraints of the model used, analysis of the force–distance data gives values for the sample Young's modulus, adhesion force, sample height, tip radius, and contact radius (or contact area) at each point.

Analysis of Current–Voltage Data. Quantitative analysis of current–voltage data requires conversion from current to current density and, hence, requires knowledge of the contact area between tip and sample. Figure 4 highlights the importance of calculating an accurate contact area. Figure 4a shows the values of the contact area extracted from fitting force–distance data, plotted against the current measured at 5 V. Each of the 400 points corresponds to a distinct point

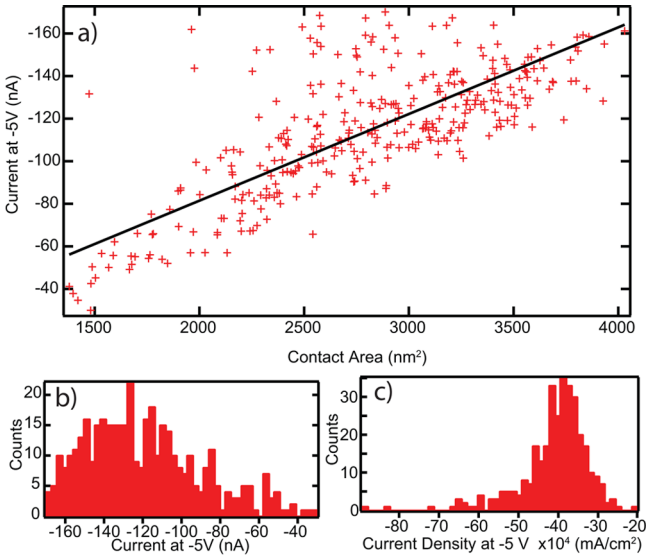

Figure 4. (a) Calculated contact area in many JKR fittings compared to the current measured at 5 V. (b) Histogram of the measured current at 5 V. (c) Histogram of current values scaled to current density using the calculated contact area.

(pixel) on the same sample; at each of these, a force–distance curve and a set of current–voltage curves were taken. Each of the current points in Figure 4a corresponds to the average current at 5 V of the 10 $I-V$ curves measured at that position. The points were arranged in a force–volume grid array. Figure 4a,b shows a large spread in the current data, with the current varying by a factor of 5 within this data set. However, there is a clear linear relation between the extracted current and the measured contact area. Consequently, the current density (Figure 4c), which takes into account the measured contact area, has a much smaller spread of approximately a factor of 2. For comparison, the contact area calculated for the known tip diameter of 30 nm, assuming a circular contact area, would be 2800 nm^2, yielding current density values that are typically a factor of 2–3 times larger. Thus, using the force–distance data to quantify the contact area in this way significantly increases the precision and accuracy of the current density data obtained.

At each point, the 10 $I-V$ curves are averaged to reduce noise, offsets are corrected (see Supporting Information section S3), and the current is converted to current density. A typical resultant $J-V$ curve is shown in the Figure 5 inset. As explained

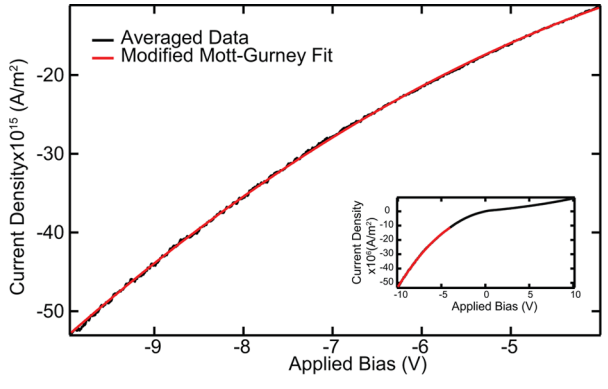

Figure 5. Average of 10 curves fitted with a modified Mott–Gurney model (red line); the inset here shows the region fitted.

DOI: 10.1021/acs.jpcc.5b02197
J. Phys. Chem. C 2015, 119, 11459–11467

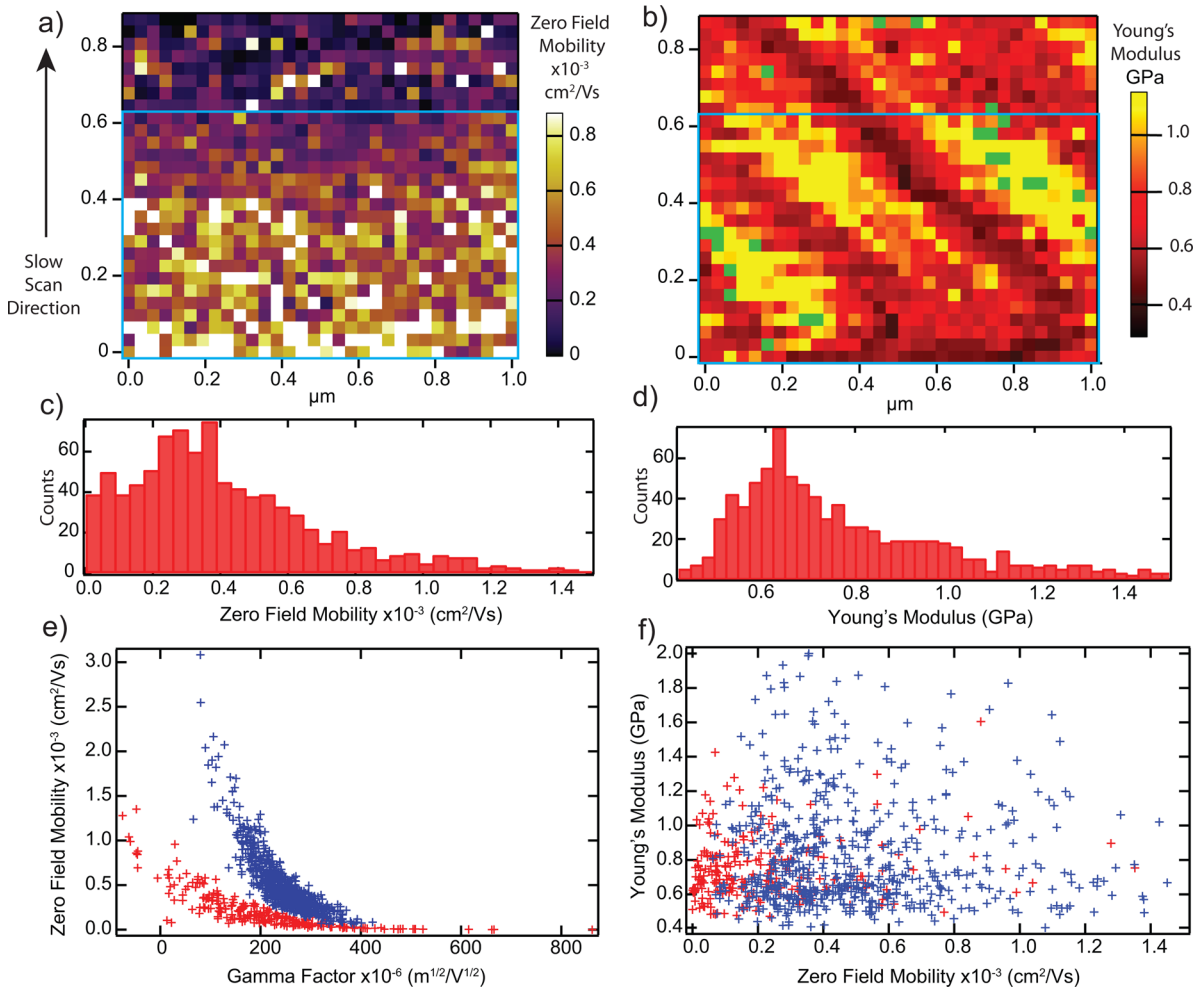

Figure 6. High resolution FVBS electrical and mechanical maps of untreated P3HT at 30 °C, showing spatially resolved (a) mobility and (b) sample Young's modulus values. Panels c and d show the distribution of mobility and modulus values, respectively. The values for zero field mobility, μ_0, are plotted against the simultaneously derived field dependence of mobility, γ, in (e) and the sample Young's modulus, E_s, in (f); the blue points are from pixels within the blue boxes shown in (a) and (b), and the red points are from the remaining upper portions of those images.

above, the response is asymmetric with higher current at negative bias, which is consistent with hole transport and a more ohmic contact at the Pt tip. For analysis, we consider only the negative bias regime.

For planar electrodes, the $J-V$ behavior of organic semiconductors is well established. At low bias (low field), the current is injection-limited, resulting in ohmic behavior ($J \propto V$). At intermediate field, the current is said to be trap limited, with $J \propto V^p$ where $p > 2$. At high field, the current should make a transition into a space-charge-limited current (SCLC) regime where $J \propto V^2$ in accordance with the Mott–Gurney model.[27]

The situation is more complicated in cAFM, in which the electrodes are no longer planar and, hence, the electric field is not uniform. The resultant current densities are much higher than those for bulk devices, leading to anomalously high mobilities when the Mott–Gurney model for bulk devices is used to fit the cAFM data. Reid et al. used finite element modeling to account for the effects of the nonlocal field,[17] proposing a semiempirical modified Mott–Gurney equation for space-charge-limited current in cAFM that incorporates the field dependence of the mobility:

$$J = \alpha\epsilon\epsilon_0\mu_0 e^{0.89\gamma(V/L)^{1/2}}\frac{V^2}{L^3}\delta_J\left(\frac{L}{2r_c}\right)^{1.6\pm0.1} \quad (4)$$

where ϵ_0 and ϵ are the vacuum permittivity and the relative permittivity of the thin film, respectively, μ_0 is the zero field mobility, γ is the strength of the field dependence of the mobility, and L is the thickness of the semiconductor thin film. α is the prefactor determined by Reid et al. from the finite element modeling to account for the nonuniform electrical field (α = 8.2 in place of 9/8 for the Mott–Gurney law for planar electrodes). The factor $\mu_0 e^{0.89\gamma(V/L)^{1/2}}$ accounts for the electric field dependence of the mobility.[28] The constant $\delta_J = 7.8 \pm 1$ was included to empirically account for the difference between mobilities derived by Reid et al. from cAFM measurements and those from planar electrodes. Note that for the contact radius, r_c, Reid et al. used an estimate based on the size of the tip. Due to deformation of the sample and the adhesion forces between tip and sample, the actual contact area is likely to be significantly larger than the estimate on the sole basis of the nominal tip radius; for the force and tip used by Reid et al., the estimated actual contact area using eq 3 would be ~6 times larger than their estimate. Comparison with the results presented here suggests that correct quantification of the

DOI: 10.1021/acs.jpcc.5b02197
J. Phys. Chem. C 2015, 119, 11459–11467

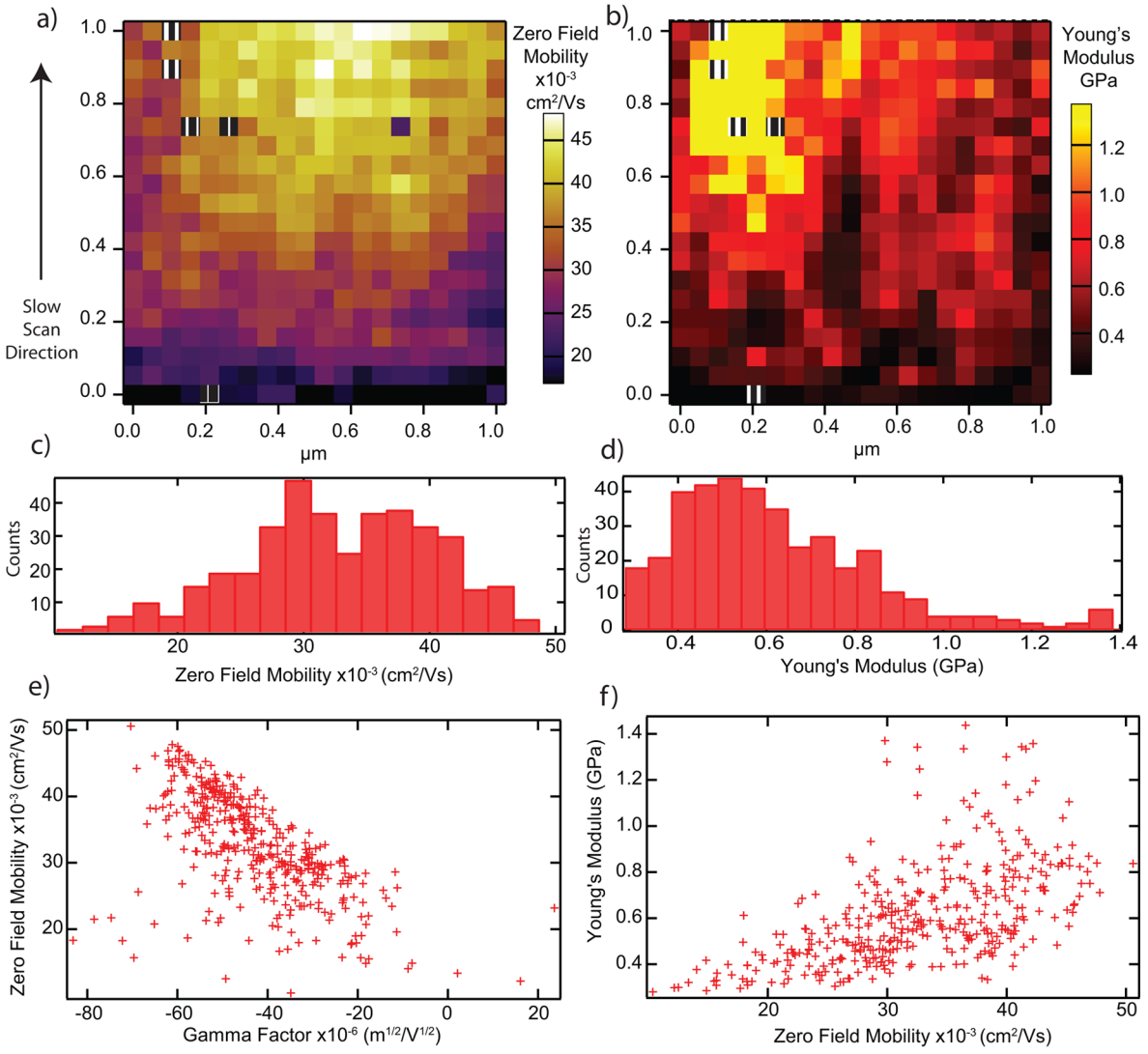

Figure 7. High resolution map of annealed P3HT at 130 °C showing (a) the mobility and (b) the sample Young's modulus across a 1 μm^2 area of surface. Panel c shows the correlation between these two parameters.

contact area obviates the need for the extra empirical scaling factor, so in the results presented below, $\delta_J = 1$ was assumed.

Figure 5 shows the results of fitting the modified Mott–Gurney equation to the average current density versus voltage curve acquired at a single point. The data are fitted in the high voltage regime, where space-charge-limited current is expected, and at negative bias, where the tip–surface contact gives an ohmic injection of holes as required for SCLC.[29] The two fitting parameters are the zero field mobility, μ_0, and the strength of the field dependence of the mobility, γ. The zero field mobility from the fit in Figure 5 is $\mu_0 = 2.50 \times 10^{-3}$ $cm^2/(V{\cdot}s)$, with $\gamma = -6.62 \times 10^{-5}$ $m^{1/2}/V^{1/2}$. This is consistent with the results of Kline et al., whose room temperature thin film measurements on 30 kDa P3HT (similar to the 25 kDa P3HT used here) found mobilities of $\mu_0 = 8 \times 10^{-3}$ $cm^2/(V{\cdot}s)$.[11] For P3HT the measured mobility depends greatly on the method of preparation, the molecular weight, and the regioregularity of the material. However, here, without the use of empirical scaling factors, values close to those reported for the bulk devices are obtained. Analysis of the current–voltage data thus gives quantitative values for the zero field mobility and the strength of the field dependence of the mobility at each point. Importantly, these data are coincident with, and simultaneous to, the mechanical property information derived from the analysis of the force–distance data.

Correlating Electrical to Mechanical Properties. Figure 6 illustrates the importance of high spatial resolution when measuring electrical and mechanical properties of polymer thin films. The untreated P3HT, measured at 30 °C, shows heterogeneity in both the mobility and the sample Young's modulus across a 1 μm^2 area. As the histograms show (Figure 6c,d), broad distributions are found for both, with the values of mobility varying by around an order of magnitude and the values of the sample Young's modulus varying by around a factor of 3. There are clear spatial correlations, i.e., patches of high or low mobility or stiffness, which indicate that the variation is real and due to local changes in material properties rather than random fluctuations.

The mechanical and electrical measurements are taken simultaneously at each point, allowing the investigation of correlations between them. Parts e and f of Figure 6 show the zero field mobility plotted against γ and against sample Young's modulus, respectively, with each point on the graphs corresponding to a distinct spatial location on the sample (or

DOI: 10.1021/acs.jpcc.5b02197
J. Phys. Chem. C 2015, 119, 11459–11467

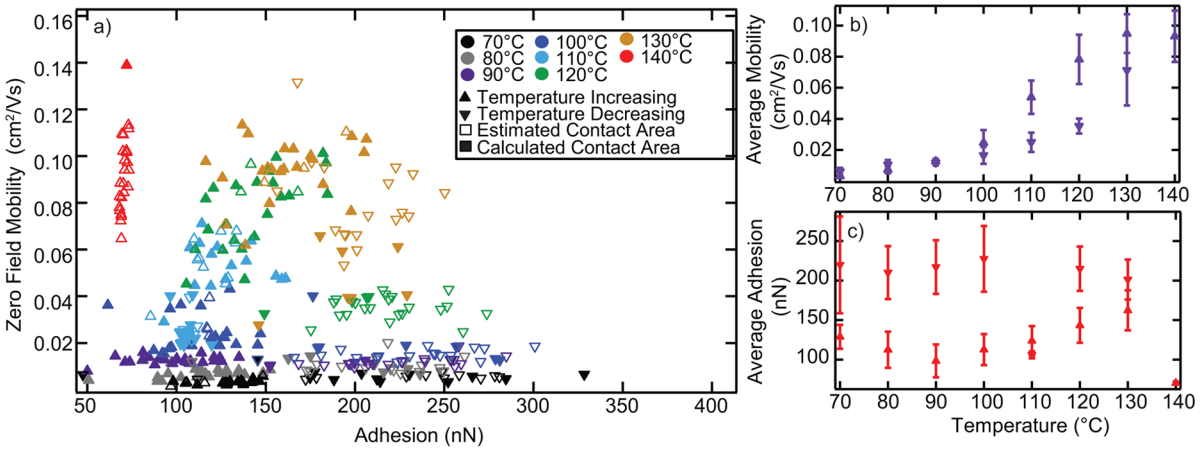

Figure 8. (a) Temperature dependence of zero field mobility and surface adhesion when unannealed P3HT is heated from 70 to 140 °C and then cooled to the original temperature. Closed symbols use a mobility calculated from a measured contact area, and open symbols have an estimated contact area. An array of 25 points was measured at each temperature. (b, c) Averaged values of zero field mobility and surface adhesion, respectively, as a function of temperature. Upward triangles signify an increase in temperature. Error bars here represent the standard deviation of the data.

equivalent pixels in Figure 6a,b). The comparison between mobility and γ shows that the data lie on two distinct trend lines, emphasized by some of the points being shown in red and some in blue; for both sets, γ increases as the mobility decreases, which is consistent with increased trapping resulting in lower mobility. The blue data points come from the region marked by the blue boxes in Figure 6a,b, with the red points coming from the upper portion of the images. Note that the scan direction is from the bottom to the top of the image. The comparison between the mobility and the sample Young's modulus maps as well as the consideration of the correlation between γ and mobility suggest that the tip condition changed around the top of the blue box. This shows how acquiring large data sets and checking the correlations between them can give more information and hence enable more reliable determination of material properties.

Considering only the measurements within the blue box, for the untreated P3HT measured at 30 °C we find average values of mobility of $5.1 \pm 0.1 \times 10^{-4}$ cm^2/(V·s) and values of sample Young's modulus of 0.86 ± 0.02 GPa. (Note that incorporating the systematic uncertainty due to calibration of the spring constant of the AFM cantilever, 5%, leads to an additional uncertainty of ~5% on these values when comparing them to other measurements, but it does not affect comparisons within the data set.)

From the graph of sample Young's modulus plotted against mobility, Figure 6f, no clear correlation between stiffness and mobility is apparent. The electrical measurements rely on conduction through the thin film, and the mechanical measurements probe the surface and near subsurface. Hence, the lack of correlation suggests that the structural variations are occurring over length scales shorter than the thickness of the film. This is supported by the observation that the derived mobility values appear to change over length scales less than 100 nm, i.e., less than the film thickness.

For comparison, Figure 7 displays the corresponding results for an annealed P3HT sample measured at 130 °C. Again there is a broad distribution of mobility and sample Young's modulus values, with clear spatial correlations demonstrating that they reflect real variations in material properties. However, the spatial variations are more smoothly varying (i.e., longer range), suggesting that the length scales of the structural variations are longer at this higher temperature after annealing.

An obvious additional feature is that both the mobility and the sample Young's modulus increase over time for this data set (note that the slow scan direction, and hence time, goes from bottom to top). It is not clear whether this is a feature of this region of the sample or of changes in the film due to prolonged annealing at this temperature, but it does show a clear correlation between mobility and stiffness that is also apparent in the scatter plot in Figure 7f. Interestingly, at this higher temperature on an annealed sample the correlation between zero field mobility and γ is less pronounced (Figure 7e), suggesting that under these conditions the transport is less trap-dominated. The increase in mobility is surprising and significant because with air sensitive materials such as P3HT, degradation over time tends to decrease the mobility. The rate of degradation is reduced here by measuring it in a nitrogen environment, which increases the characteristic degradation time (time over which the mobility decreases by a factor of e) from under 1 h in air to over 10 h (see section S3 in the Supporting Information), sufficient for these measurements.

From the results shown in Figures 6 and 7, a direct comparison can be made between the room temperature behavior and the high temperature behavior of P3HT. At 130 °C, the average mobility has increased by almost an order of magnitude to $32.6 \pm 0.4 \times 10^{-3}$ cm^2/(V·s) while the sample Young's modulus has decreased by more than 20% to 0.69 ± 0.02 GPa. Note that these measurements were taken with different tips and on different samples, but due to the large data sets, these changes are statistically significant. Complete sets of maps for both data sets, showing all the parameters determined from FVBS, are given in section S4 of the Supporting Information. The analysis of the correlations between the multiple material properties measured by this technique can give further insight into the material's behavior.

Temperature-Dependent Mapping of P3HT. Using a smaller data set at each temperature to minimize the effects of degradation, the temperature dependence of the nanoscale electrical and mechanical properties of P3HT were investigated between 70 and 140 °C, with 140 °C being the standard annealing temperature for P3HT.[3,30] The resultant changes in zero field mobility and adhesion are shown in Figure 8. The

DOI: 10.1021/acs.jpcc.5b02197
J. Phys. Chem. C 2015, 119, 11459−11467

mobility shows a consistent increase with temperature, evident in both (a) and (b) of Figure 8. Despite the smaller data sets at each temperature, these measurements took roughly an hour per temperature point (including the delay at each temperature to reach thermal equilibrium) and roughly 20 h in total. Figure 8 shows the measured mobility to be lower as the sample is cooled in comparison with the values measured at the same temperature as the sample was heated; however, this can be attributed to sample degradation. Taking account of the expected rate of degradation (see section S3 in the Supporting Information), this suggests that the mobility as the sample was cooled was effectively higher than that during heating, consistent with a small increase in mobility due to annealing. However, we cannot give a statistically robust determination of the changes in mobility due to annealing from this data. Plotting the mobility data on a logarithmic scale (see section S5 in the Supporting Information) shows that up to around 120 °C the mobility exponentially decreases with inverse temperature, suggesting that over this temperature range transport occurs via a hopping mechanism.[31] At 140 °C the adhesion drops dramatically, the sample becomes more uniform, and the rate of increase of mobility with temperature dramatically decreases. The field dependence of the mobility, γ, also decreases, with increased mobility with rising temperature (see section S5 in the Supporting Information).

Kline et al. studied the dependence of charge carrier mobility, measured in a thin film transistor geometry in the saturation regime, on the molecular weight of P3HT.[11] They found that high molecular weight (defined by them as >30 kDa) P3HT showed only relatively small increases in mobility upon annealing, and low molecular weight (defined by them as <4 kDa) P3HT was more sensitive to processing conditions and had lower mobility but could show larger increases upon annealing. Analysis of the temperature dependence of the mobility and of the thin film structures led to their conclusion that in low and medium molecular weight P3HT films, mobility was limited by domain boundaries within the film. For the low, medium, and high molecular weight films, they found that transport was thermally activated below room temperature. The results shown here in Figure 8 are consistent with such a thermally activated transport process, persisting above room temperature until a transition occurs at around 130 °C, which we speculate is due to a change in structure that reduces the grain boundaries within the film.

CONCLUSIONS

We have demonstrated that nanoscale electrical and mechanical properties of organic semiconductor thin films can be quantitatively and simultaneously acquired by AFM. For P3HT, both the electrical and the mechanical properties are heterogeneous at submicron length scales and depend strongly on temperature. From room temperature up to around 110 °C, the electrical properties of P3HT are found to be consistent with a grain boundary limited transport model, showing a roughly exponential decrease in mobility with inverse temperature. At higher temperatures, around 130 °C, the $I-V$ characteristics suggest a less trap-dominated behavior, the length scale of spatial variations in mobility increases, and a correlation between sample stiffness and mobility becomes evident, suggesting an increase in order in the film.

The FVBS measurement technique demonstrated here should be broadly applicable to the study of thin film organic semiconductors. FVBS is suited to studying through film transport in planar geometries and hence is of particular relevance for materials of interest for OPV and OLED applications. For these applications, devices are often operated above room temperature; the significant changes in material properties at raised temperatures makes it essential that the materials are studied under realistic operating conditions, as shown here. Measurements are made without a top contact in FVBS, making it ideal for studying the effects of processing parameters on material performance.

ASSOCIATED CONTENT

Supporting Information

Procedures for calibration and data processing, analysis of sample degradation due to air exposure, further data from FVBS measurements, and further analysis of the temperature dependence of the mobility are provided. The Supporting Information is available free of charge on the ACS Publications website at DOI: 10.1021/acs.jpcc.5b02197.

AUTHOR INFORMATION

Corresponding Author

*N.R.W. E-mail: Neil.Wilson@warwick.ac.uk.

Notes

The authors declare no competing financial interest.

ACKNOWLEDGMENTS

Oxford Instruments Asylum Research is thanked for their support. We thank EPSRC for support through a studentship for D.W. (EP/K503204/1). I.H. is supported by the TSB project "Development of Prototype High Efficiency Multi-Junction Organic Solar Cells" (no. 100900). The authors acknowledge the University of Warwick Research Technology Platform (Electron Microscopy) for assistance in the research described in this paper. We thank Mark Skilbeck and Tom Howells for assistance with implementing fitting algorithms.

REFERENCES

(1) MacDonald, G. A.; Veneman, P. A.; Placencia, D.; Armstrong, N. R. Electrical Property Heterogeneity at Transparent Conductive Oxide/Organic Semiconductor Interfaces: Mapping Contact Ohmicity Using Conducting-Tip Atomic Force Microscopy. *ACS Nano* **2012**, *6*, 9623−9636.

(2) Collins, B. A.; Tumbleston, J. R.; Ade, H. Miscibility, Crystallinity, and Phase Development in P3HT/PCBM Solar Cells: Toward an Enlightened Understanding of Device Morphology and Stability. *J. Phys. Chem. Lett.* **2011**, *2*, 3135−3145.

(3) Dang, M. T.; Hirsch, L.; Wantz, G. P3HT:PCBM, Best Seller in Polymer Photovoltaic Research. *Adv. Mater.* **2011**, *23*, 3597−3602.

(4) Mok, S. M.; Yan, F.; Chan, H. L. W. Organic Phototransistor Based on Poly(3-hexylthiophene)/TiO_2 Nanoparticle Composite. *Appl. Phys. Lett.* **2008**, *93*, 023310.

(5) Jia, H.; Gowrisanker, S.; Pant, G. K.; Wallace, R. M.; Gnade, B. E. Effect of Poly (3-hexylthiophene) Film Thickness on Organic Thin Film Transistor Properties. *J. Vac. Sci. Technol., A* **2006**, *24*, 1228−1232.

(6) Kline, R.; McGehee, M.; Kadnikova, E.; Liu, J.; Fréchet, J. Controlling the Field-Effect Mobility of Regioregular Polythiophene by Changing the Molecular Weight. *Adv. Mater.* **2003**, *15*, 1519−1522.

(7) Himmelberger, S.; Vandewal, K.; Fei, Z.; Heeney, M.; Salleo, A. Role of Molecular Weight Distribution on Charge Transport in Semiconducting Polymers. *Macromolecules* **2014**, *47*, 7151−7157.

(8) Li, G.; Shrotriya, V.; Yao, Y.; Yang, Y. Investigation of Annealing Effects and Film Thickness Dependence of Polymer Solar Cells Based on Poly(3-hexylthiophene). *J. Appl. Phys.* **2005**, *98*, 043704.

DOI: 10.1021/acs.jpcc.5b02197
J. Phys. Chem. C 2015, 119, 11459−11467

(9) An, L.; Duan, Y.; Yuan, Y.; Zhou, L.; Zhang, J. Effect of Thermal Annealing on the Microstructure of P3HT Thin Film Investigated by RAIR Spectroscopy. *Vib. Spectrosc.* **2013**, *68*, 40−44.
(10) Bagui, A.; Iyer, S. S. K. Increase in Hole Mobility in Poly (3-hexylthiophene-2,5-diyl) Films Annealed Under Electric Field During the Solvent Drying Step. *Org. Electron.* **2014**, *15*, 1387−1395.
(11) Kline, R.; McGehee, M.; Kadnikova, E. Dependence of Regioregular Poly (3-hexylthiophene) Film Morphology and Field-Effect Mobility on Molecular Weight. *Macromolecules* **2005**, *38*, 3312−3319.
(12) Savagatrup, S.; Printz, A. D.; Rodriquez, D.; Lipomi, D. J. Best of Both Worlds: Conjugated Polymers Exhibiting Good Photovoltaic Behavior and High Tensile Elasticity. *Macromolecules* **2014**, *47*, 1981−1992.
(13) Im, M. J.; Son, S. Y.; Moon, B. J.; Lee, G.-Y.; Kim, J. H.; Park, T. Improved Photovoltaic Performance by Enhanced Crystallinity of Poly(3-hexyl)thiophene. *Org. Electron.* **2013**, *14*, 3046−3051.
(14) Osaka, M.; Benten, H.; Lee, L.-T.; Ohkita, H.; Ito, S. Development of Highly Conductive Nanodomains in Poly(3-hexylthiophene) Films Studied by Conductive Atomic Force Microscopy. *Polymer* **2013**, *54*, 3443−3447.
(15) O'Connor, B.; Chan, E. P.; Chan, C.; Conrad, B. R.; Richter, L. J.; Kline, R. J.; Heeney, M.; McCulloch, I.; Soles, C. L.; DeLongchamp, D. M. Correlations Between Mechanical and Electrical Properties of Polythiophenes. *ACS Nano* **2010**, *4*, 7538−7544.
(16) Berger, R.; Butt, H.-J.; Retschke, M. B.; Weber, S. A. L. Electrical Modes in Scanning Probe Microscopy. *Macromol. Rapid Commun.* **2009**, *30*, 1167−1178.
(17) Reid, O. G.; Munechika, K.; Ginger, D. S. Space Charge Limited Current Measurements on Conjugated Polymer Films Using Conductive Atomic Force Microscopy. *Nano Lett.* **2008**, *8*, 1602−1609.
(18) Nikiforov, M. P.; Darling, S. B. Improved Conductive Atomic Force Microscopy Measurements on Organic Photovoltaic Materials via Mitigation of Contact Area Uncertainty. *Prog. Photovoltaics* **2013**, *21*, 1433−1443.
(19) Laby, G., Kaye, T. H. *Tables of Physical and Chemical Constants*, 15th ed.; Longman, London, U.K., 1993.
(20) Sader, J. E.; Chon, J. W. M.; Mulvaney, P. Calibration of Rectangular Atomic Force Microscope Cantilevers. *Rev. Sci. Instrum.* **1999**, *70*, 3967−3969.
(21) Hancox, I.; Sullivan, P.; Chauhan, K.; Beaumont, N.; Rochford, L.; Hatton, R.; Jones, T. The Effect of a MoO_x Hole-Extracting Layer on the Performance of Organic Photovoltaic Cells Based on Small Molecule Planar Heterojunctions. *Org. Electron.* **2010**, *11*, 2019−2025.
(22) Shrotriya, V.; Li, G.; Yao, Y.; Chu, C.-W.; Yang, Y. Transition Metal Oxides as the Buffer Layer for Polymer Photovoltaic Cells. *Appl. Phys. Lett.* **2006**, *88*, 073508.
(23) Butt, H.-J.; Cappella, B.; Kappl, M. Force Measurements with the Atomic Force Microscope: Technique, Interpretation and Applications. *Surf. Sci. Rep.* **2005**, *59*, 1−152.
(24) Grant, C. A.; Alfouzan, A.; Gough, T.; Twigg, P. C.; Coates, P. D. Nano-Scale Temperature Dependent Visco-Elastic Properties of Polyethylene Terephthalate (PET) using Atomic Force Microscope (AFM). *Micron* **2013**, *44*, 174−178.
(25) Alexeev, A.; Loos, J.; Koetse, M. M. Nanoscale Electrical Characterization of Semiconducting Polymer Blends by Conductive Atomic Force Microscopy. *Ultramicroscopy* **2006**, *106*, 191−199.
(26) Tahk, D.; Lee, H. H.; Khang, D. Y. Elastic Moduli of Organic Electronic Materials by the Buckling Method. *Macromolecules* **2009**, *42*, 7079−7083.
(27) Chiguvare, Z.; Dyakonov, V. Trap-Limited Hole Mobility in Semiconducting Poly(3-hexylthiophene). *Phys. Rev. B: Condens. Matter Mater. Phys.* **2004**, *70*, 235207.
(28) Pasveer, W.; Cottaar, J.; Tanase, C.; Coehoorn, R.; Bobbert, P.; Blom, P.; de Leeuw, D.; Michels, M. Unified Description of Charge-Carrier Mobilities in Disordered Semiconducting Polymers. *Phys. Rev. Lett.* **2005**, *94*, 206601.
(29) Chirvase, D.; Chiguvare, Z.; Knipper, M.; Parisi, J.; Dyakonov, V.; Hummelen, J. C. Temperature Dependent Characteristics of Poly(3-hexylthiophene)-Fullerene Based Heterojunction Organic Solar Cells. *J. Appl. Phys.* **2003**, *93*, 3376−3383.
(30) Ma, W.; Yang, C.; Gong, X.; Lee, K.; Heeger, A. J. Thermally Stable, Efficient Polymer Solar Cells with Nanoscale Control of the Interpenetrating Network Morphology. *Adv. Funct. Mater.* **2005**, *15*, 1617−1622.
(31) Coropceanu, V.; Cornil, J.; da Silva Filho, D. A.; Olivier, Y.; Silbey, R.; Brédas, J.-L. Charge Transport in Organic Semiconductors. *Chem. Rev.* **2007**, *107*, 926−952.

DOI: 10.1021/acs.jpcc.5b02197
J. Phys. Chem. C 2015, 119, 11459−11467